

Biomedical Paper

A C-Arm Fluoroscopy-Guided Progressive Cut Refinement Strategy Using a Surgical Robot

Jianhua Yao, M.S., Russell H. Taylor, Ph.D., Randal P. Goldberg, M.S., Rajesh Kumar, M.S., Andrew Bzostek, M.S., Robert Van Vorhis, Ph.D., Peter Kazanzides, Ph.D., and Andre Gueziec, Ph.D.

Departments of Computer Science (J.Y., R.H.T., R.K., A.B.) and Mechanical Engineering (R.P.G.), The Johns Hopkins University, Baltimore, Maryland; Integrated Surgical Systems, Davis, California (R.V.V., P.K.), and IBM T.J. Watson Research Center, Yorktown Heights, New York (A.G.)

ABSTRACT We describe a new method to cut a precise, high-quality femoral cavity in Revision Total Hip Replacement surgery (RTHR) using a surgical robot and an intra-operative C-arm fluoroscope. With respect to previous approaches, our method contains several new features. (1) We describe a novel checkerboard plate designed to correct the geometric distortion within fluoroscopic images. Unlike previous distortion correction devices, the plate does not completely obscure any part of the image, and the distortion correction algorithm works well even when there are some overlaid objects in the field of view. (2) Also included are a novel corkscrew fiducial object designed to be integrated with the robot end-effector, and a 6D pose estimation algorithm based on the two-dimensional (2D) projection of the corkscrew, used in robot-imager registration and imager co-registration. (3) In addition, we develop a cavity location algorithm, which utilizes image subtraction and 2D anatomy contour registration techniques. (4) Finally, we propose a progressive cut refinement strategy, which progressively improves the robot registration during the procedure. We have conducted several experiments, in both simulated and *in vitro* environments. The results indicate that our strategy is a promising method for precise orthopedic procedures like total hip replacement. *Comp Aid Surg* 5:373–390 (2000). ©2001 Wiley-Liss, Inc.

Key words: C-arm fluoroscopy guidance, cut refinement, image registration, surgical robot

INTRODUCTION

This paper describes novel techniques permitting the use of portable fluoroscopic C-arms for intra-operative localization and guidance in robotically assisted orthopaedic surgery. Specifically, our goal is to direct the robot to cut a precisely defined shape in a bone that has been located in C-arm images without requiring additional navigation equipment such as an optical tracking system. Instead, we

emphasize the use of feedback from the images themselves to provide robust registration and adaptation to residual calibration errors.

Our research is part of a joint project with Integrated Surgical Systems (ISS) to develop a computer-integrated system to assist surgeons in Revision Total Hip Replacement surgery (RTHR). RTHR is performed after a patient has had PTHR

Received November 1, 1999; accepted November 15, 2000.

Address correspondence/reprint requests to: Jianhua Yao, NEB 224, Department of Computer Science, The Johns Hopkins University, Baltimore, MD 21218, USA; Telephone: (410) 516-4057; E-mail: jhyao@cs.jhu.edu.

©2001 Wiley-Liss, Inc.

(Primary Total Hip Replacement surgery) and the implant has failed for some reason. RTHR is a much more difficult operation, because less bone tissue remains and a precise, high-quality cavity is required. In 1992, 27,000 RTHR procedures were performed in the U.S. The average cost per procedure was \$23,774, with an average hospital stay of 10.9 days.¹

In standard (manual surgery) practice, THR procedures are planned qualitatively with standard X-ray images and acetate overlays to select a few likely implant sizes and models. In surgery, the femoral head (in the case of PTHR) or the implant (in the case of RTHR) is removed. In the case of RTHR, hand-held instruments are used to remove the cement left behind, often with the assistance of fluoroscopic X-rays. A final implant choice is made, and hand-held tools are used to prepare a slightly larger femoral cavity. In both PTHR and RTHR, manual techniques for preparing the implant cavity leave a great deal to be desired. In RTHR, the primary concerns with the manual method include the duration of the procedure, the high rate of complications (primarily fractures), and the accuracy of alignment of the implant.

A surgical robot can be used to safely mill a precise cavity for the femoral implant. There are currently two clinically applied systems for THR: the ISS ROBODOC® system^{2,3} and the CASPAR system.⁴ The ISS ROBODOC systems have been used successfully in over 6,000 interventions, including about 50 RTHR cases, without any fractures or other serious complications due to the robot.² In these systems, the implant cavity is planned from preoperative CT images, the robot is registered to the patient, and the robot cuts the cavity. The current ROBODOC RTHR procedure^{1,5} is similar to that for PTHR. The main difference is the specialized software for locating the cement mantle around the implant and for defining a customized cavity to ensure that all cement is removed. Although this process has worked well in many cases, there are several limitations. First, CT imaging artifacts can make the preoperative planning difficult. Second, it is not always easy to predict what will happen when the implant is removed. These considerations have led us to explore alternative imaging approaches that are compatible with intra-operative planning and assessment.

Accurate robot-to-patient and robot-to-imager registrations are essential to RTHR surgery. Indeed, the smaller amount of cortical bone remaining and the generally larger implant sizes used in revision cases make the requirement if anything

more stringent. The robot's relative accuracy is extremely good, and the cavity shape will match the implant shape to better than 0.1 mm. The registration requirement is to guarantee that the cavity is placed within about $\delta = 0.5\text{--}1.0$ mm of its preplanned position, i.e., that the actual cavity have a shape accuracy of 0.1 mm and be placed within an envelope δ larger than the shape.

Currently, implanted fiducial pins^{2,6} are used for RTHR registrations, and either implanted pins or a pinless 3D-3D technique⁷ are used for PTHR. More generally, there has been considerable work on 3D-3D and 2D-3D registration methods for computer-integrated surgery (e.g., References 8–16). Among registration techniques, image-based methods are desirable because they are less invasive, but they present significant technical challenges. 2D-3D methods are attractive for intra-operative use since they require more readily available intra-operative imaging equipment (a single C-arm fluoroscope). Lavallée et al.⁸ registered 2D images to 3D solid anatomical models. They used a hierarchical data structure to quickly query the closest point from anatomy surface to X-ray paths. Hamadeh et al.⁹ extended this work by using cooperation between 2D-3D registration and 2D segmentation. Guezic et al.^{10–12,17,18} explored the feasibility of anatomy-based registration using fluoroscopy. They proposed a 2D to 3D registration algorithm that employed the apparent contour of the 3D surface and the registration between a set of 3D points and 3D lines. They also extended the “NPBS” method¹⁹ to provide a direct registration of the robot to fluoroscopic image space. Two significant differences from traditional “NPBS” are (1) the use of thin plate splines²⁰ for de-warping interpolations and (2) the technique for obtaining images of multiple known calibration points. They employed a radiolucent probe placed into the cutter collet of the robot. This probe was swept through two planes to construct a “virtual” calibration grid. Experiments showed that this method was quite accurate, permitting 3D localization of a robot within 0.1–0.4 mm with a conventional C-arm fluoroscope.¹¹ The initial motivation for the work reported in this paper was the development of a fast and non-invasive registration method for RTHR that would be potentially applicable to PTHR and other orthopaedic interventions.

Our goal is the development of a system that permits planning of the implant cavity shape and position with either preoperative CT images or multiple X-ray images.¹ In the CT-based scheme, the surgeon manipulates the cavity shape and po-

sition in CT coordinates and the system essentially predicts what a CT of the patient might look like after the cavity is cut and the implant is placed into the bone. ORTHODOC® is the preplanning tool for ROBODOC® using preoperative CT.²¹ In the case where multiple fluoroscopic images are used, an “image spreadsheet” is set up after the co-registration of these images.¹ The planning system uses graphic overlays to predict what fluoroscopy images would look like after the cavity is cut and the implant placed. The co-registration between fluoroscopic images can be obtained virtually using an external tracking device^{22–26} as in virtual fluoroscopy systems, or it can be obtained using the image-based method proposed in our paper (see section entitled *C-arm pose estimation and extrinsic calibration*).

Fluoroscopy image-based intra-operative planning is attractive because: 1) it does not require a CT scan, so it requires one less procedure; 2) the artifacts present in preoperative CT of an RTHR procedure will not be present in the planning images; 3) the previously separate steps of registering the robot to the planning images and to the fluoroscope are now performed in a single intra-operative calibration step; 4) the planning can be done after the implant and cement are removed, which makes the procedure more accurate; and 5) the planning based on intra-operative data captures the most current patient anatomy information. Planning based on multiple fluoroscopic images also presents many challenges. First, the co-registration between images must be done very accurately. Second, the selection of fluoroscopic images and the planning on a 2D base requires a lot of surgeon experience. In addition, since the planning is now done intra-operatively, the software and image acquisition procedure must be designed so that a significant amount of OR time, and its associated costs, are not added onto the procedure.

Our development of a computer-integrated RTHR system started about five years ago. Taylor, Joskowicz et al.^{1,5} proposed the initial system. Some of their ideas have been investigated in the current research. Guezic et al.^{10–12,17,18} explored the feasibility of anatomy-based registration using fluoroscopy. The goal of our research is to direct the robot to cut a precise cavity using intra-operative portable C-arm fluoroscopy as guidance. We propose a series of new methods and a system to solve this image-based registration problem without requiring additional equipment such as optical tracking systems. We also propose a progressive cutting strategy using image feedback to improve the system accuracy.

The Methods section begins with an overview of the system. This is followed by a description of the C-arm intrinsic and extrinsic calibration, including a new method for fluoroscopic image spatial distortion correction and a novel pose estimation device for computing robot-to-imager and imager pose-to-pose transformations. Simple cutting experiments utilizing these techniques are then described, followed by a description of a cavity location algorithm. Next, to improve the final robot-bone registration, a progressive cut refinement strategy is presented, along with cutting experiments using both real and simulated images. In the last section of the paper, we discuss these results and our future plans.

METHODS AND RESULTS

System Overview

The flow chart in Figure 1 illustrates the outline of our system. First, the shape and place of the cut cavity is planned based on the preoperative CT volume or multiple X-ray images of the femur. During the preoperative setup, a corkscrew-shaped fiducial object is mounted on the robot end-effector and a calibration procedure is performed to determine the corkscrew-to-robot transformation (see section entitled *C-arm pose estimation and extrinsic calibration*). In the intra-operative stage, the femur is placed in a fixation device that holds it in a fixed but unknown position relative to the robot. Multiple C-arm images are acquired. The registration between robot, patient and imager is determined using our pose estimation algorithm and the 2D-3D anatomy- or fiducial-based registration method. A shape is then cut based on the registration. After cutting, another set of images is taken in C-arm poses similar to those used for initial registration. The cut cavity image is detected using a digital subtraction technique and the cavity position is compared to the planned cavity (see *Cavity Location Algorithm* section). The registration between the robot and patient is then updated based on the discrepancy between the cut cavity and the planned cavity, and the preoperative plan is also updated accordingly. The procedure is iterated until we get the final cut. After the surgery, follow-up validation can be performed using postoperative images.

We have demonstrated our method experimentally on dental acrylic phantoms and on simulated images. Figure 2 shows a typical experimental setup. The de-warping plate is placed over the C-arm detector, and the corkscrew for pose estimation is attached to a ROBODOC® cutter. A dental

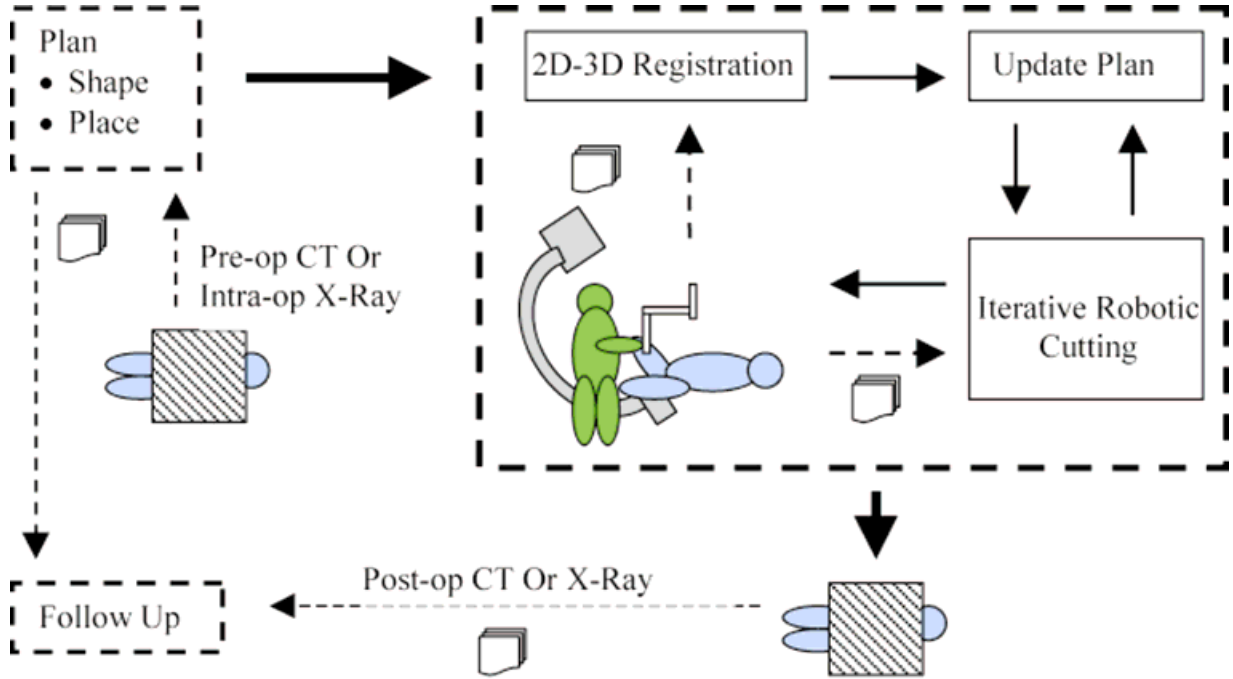


Fig. 1. System flow chart.

acrylic phantom held by a box holder is used for these cutting experiments to evaluate our method. The advantage of an acrylic phantom is that it gives us a relatively simple and repeatable means for assessing the bottom-line accuracy of the system.

C-Arm Calibration and Pose Estimation

The C-arm can be characterized approximately as a perspective pinhole camera. The calibration goal is to find the transformation between 3D world coordinates and 2D C-arm image coordinates. There are four steps to transforming a

point in 3D world coordinates to 2D C-arm image coordinates.²⁷

Step 1: Rigid transformation from the world coordinate system (x_w, y_w, z_w) to the C-arm coordinate system (x_c, y_c, z_c) :

$$\begin{pmatrix} x_c \\ y_c \\ z_c \end{pmatrix} = R \begin{pmatrix} x_w \\ y_w \\ z_w \end{pmatrix} + T \tag{1}$$

where R is a 3*3 rotation matrix and T is a 3 translation vector.

Step 2: Transformation from 3D C-arm coordinate (x_c, y_c, z_c) to undistorted image coordination (x_u, y_u) using perspective projection with pinhole camera geometry.

$$x_u = f \frac{x_c}{z_c}, \quad y_u = f \frac{y_c}{z_c} \tag{2}$$

where f is the effective focal length.

Step 3: Spatial distortion on image coordination which maps (x_u, y_u) to (x_d, y_d) .

$$(x_d, y_d) = M(x_u, y_u), \tag{3}$$

where $M(x, y)$ is the distortion mapping function.

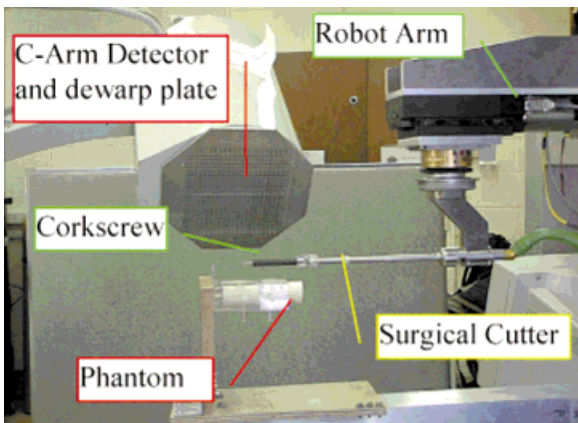


Fig. 2. Experimental setup.

Step 4: Physical image coordinate (x_d, y_d) to computer image coordinate (x_f, y_f) transformation.

$$x_f = \frac{x_d}{p_x} + c_x, \quad y_f = \frac{y_d}{p_y} + c_y \quad (4)$$

where (p_x, p_y) is the pixel scaling on the image base and (c_x, c_y) is the image center.

The parameters used in these four steps can be categorized into two classes:

1. *Intrinsic Parameters.* The effective focal length, or image plane to projective center distance, f ; the image center, (c_x, c_y) ; the pixel scaling, (p_x, p_y) ; and the distortion map, $M(x, y)$.
2. *Extrinsic Parameters.* There are six extrinsic parameters: the Euler angles yaw α , pitch β , and tilt γ for Rotation R , and the three components (T_x, T_y, T_z) for the translation vector T . The process of computing the extrinsic parameter is also called pose estimation.

The calibration method in our system will be described in the next two sections below.

Intrinsic Image Calibration

Intrinsic imaging parameters correspond to image warping, focal length, pixel scaling, and image center, and can be computed by analyzing an image of a calibration object of known geometry. The calibration method of Schreiner et al.²⁸ was used to compute the C-arm focal length, the pixel scaling, and the image center. It has been reported in the literature that the focal length may change up to several millimeters at different C-arm poses.²⁹ Currently, this change in focal length results in a change of pixel size, which is captured by the de-warping algorithm. This allows the change in focal length to be accounted for.

In general, the curved geometry of the X-ray detector causes a circular symmetric distortion, and the interaction of the electrons in the intensifier tube with the Earth's magnetic field causes an asymmetric distortion. Thus, the C-arm exhibits differing but repeatable distortions at different poses. Using fluoroscopic X-ray imaging for quantitative measurement requires precise calibration of the imager to eliminate these spatial distortions. Some researchers conducted extensive investigations on this topic. Boone et al.³⁰ provided the theory and analysis of the nature of the distortion and proposed some software techniques to correct it. Schreiner et al.²⁸ implemented Boone's method by placing a grid of radiopaque spheres over the

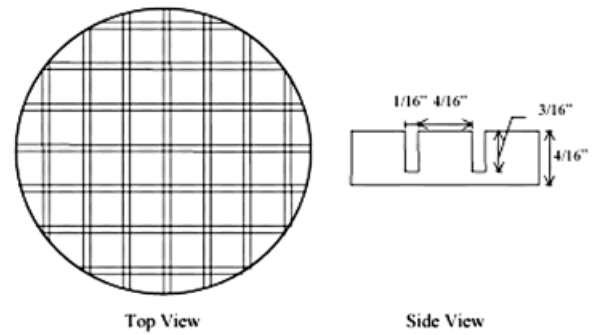


Fig. 3. De-warping plate configuration. Left: top view of plate; right: side view of plate.

C-arm detector. Fahrig et al.²⁹ also used a grid of small steel beads to correct the distortion and fit a fifth-order polynomial of distortions based on the pose of the C-arm. Yaniv et al.³¹ also reported their fluoroscopic image de-warping technique for a computer-integrated bone fracture reduction system. They used a grid of beads to generate a de-warping map of the pixels at the bead location and used bilinear interpolation to obtain the map for the rest of the pixels. Guezic et al.¹² extended the “NPBS” method to provide a method that combined the fluoroscopic image de-warping and calibration.

In our distortion correction approach, a quarter-inch thick semi-radiolucent aluminum plate is placed over the detector of the fluoroscopic C-arm (Fig. 2). Horizontal and vertical grooves 3/16" deep and 1/16" wide are machined in the plate in a square pattern at quarter-inch intervals (Fig. 3). These grooves show up as pale lines on the X-ray images, and provide enough contrast to be found in the image by our image segmentation methods. Other objects are still clearly visible with the checker pattern as background.

We can leave the plate on the detector all the time or take it off after the distortion correction. There are advantages and disadvantages to each approach. If the plate is left on, then it is possible to compensate for image distortion directly in each image. The drawback is that there may be some loss of image contrast (as with our plate) or some obscuring of image features (as with more conventional bead or wire fiducial patterns). Experiments with this system using a large smoked ham to represent the approximate radiolucent density of a human limb indicated that the loss of contrast could be accepted in some case (Fig. 4). The alternative is to pre-calibrate a few key image poses and then use this data during the actual procedure. Our experi-

ments were done with a 1970s-era C-arm (GE Polarix 2). We chose the latter approach during the cutting experiments described below, since it simplified image processing and reduced artifacts with our very old C-arm.

We have investigated various algorithms to use with this checkerboard plate to compensate for fluoroscopic image distortion. Methods examined include Piecewise Polynomial Mapping Algorithms, Thin Plate Spline Morphometric Algorithms,²⁰ and a Two-Pass Scanline Algorithm.³² Our current preferred choice outlined below is based on a variant of a Two-Pass Scanline Algorithm.

1. Image points (u_i, v_i) corresponding to the centerline of each vertical and horizontal groove are found. First, the profiles of the image density along the horizontal and vertical directions are obtained by summing up all pixel values on the horizontal and vertical scan line. Then the image space is subdivided into small square regions at the peaks of the profiles. Hence, each small square region contains only one square. In each region, the groove points are first roughly located at the peak point of image intensity between two squares, then they are refined by the constraints between groove points in neighborhood regions (smoothness, continuity, and gradient).

2. A fifth-order Bernstein polynomial is fitted to each vertical or horizontal groove using the entire set of candidate groove points found in that groove. The Bernstein polynomial is defined by Equation (5):

$$u = B(a_0, \dots, a_5; v) = \sum_{k=0}^5 a_k \binom{5}{k} (1-v)^{5-k} v^k \quad (5)$$

The fitting operation is to find the a_k to minimize the least square metric

$$\sum [u_i - B(a_0, \mathbf{k}, a_5; v_i)]^2$$

Bernstein polynomial curves have several advantages compared to regular power basis polynomial curves. They are more robust, less sensitive to noise, and have the ability to smoothly interpolate the missing part of the curve.

3. A Two-Pass Scanline Algorithm is employed to correct the image distortion.³² The first pass is responsible for re-sampling each row independently. It maps all (u, v) to their (x, y) coordinates in an intermediate image I . The second pass

then re-samples each column in I , mapping every (x, v) to its final (x, y) position.

In the first pass, for each horizontal scan line in the image, the intersections between the scan line and the vertical Bernstein-based curves found in the above steps are computed. Thus, the scan line is divided into small intervals and the intersection points are used to fit a piece-wise cubic spline using the displacements from their ideal locations. By interpolating all the pixels on the scan line using the cubic spline line, the image can be re-sampled in the horizontal direction. This process is repeated to correct the distortion of the grid in the vertical direction.

Our experience so far with this method is that it is fast and robust. Sample experimental images on smoked ham can be found in Figure 4. The figure shows the intermediate steps and result of the de-warping algorithm, and a distortion vector graph over the image space.

The accuracy of the distortion correction process was verified by following experiment. First, one image with the checkerboard plate was taken, the spatial distortion of the image was corrected, and the lookup table was saved. Next, a set of beads spaced 20 mm apart was attached over the plate, and another image was taken. The image of the beads was then de-warped using the saved lookup table. The beads were detected in the image and the distances between pairs of beads computed. Comparison of the computed distance and the known actual distance between beads gives an assessment of the accuracy of the de-warping algorithm. The mean error was 0.12 mm on the central area (approximately 120×120 mm) and 0.25 mm on the marginal area. Pixel size is approximately 0.32 mm. This shows that our distortion correction method provides reasonably accurate results.

C-Arm Pose Estimation and Extrinsic Calibration

For extrinsic calibration, the task is to compute the transformation between the C-arm coordinate system and other intra-operative coordinate systems such as the patient's anatomy, the robot, and the surgical tool. There are a number of papers that describe 2D-3D registration of C-arm images to preoperative CT.^{8-10,33} There are also several systems that combine intra-operative C-arm images with intra-operative navigation systems to assist in surgical task execution.²²⁻²⁶ Typically, those methods rely on external tracking devices such as the Optotrak[®] to determine relative changes in C-arm poses. Yaniv et al.³¹ designed a calibration object to perform C-arm calibration. The object has a

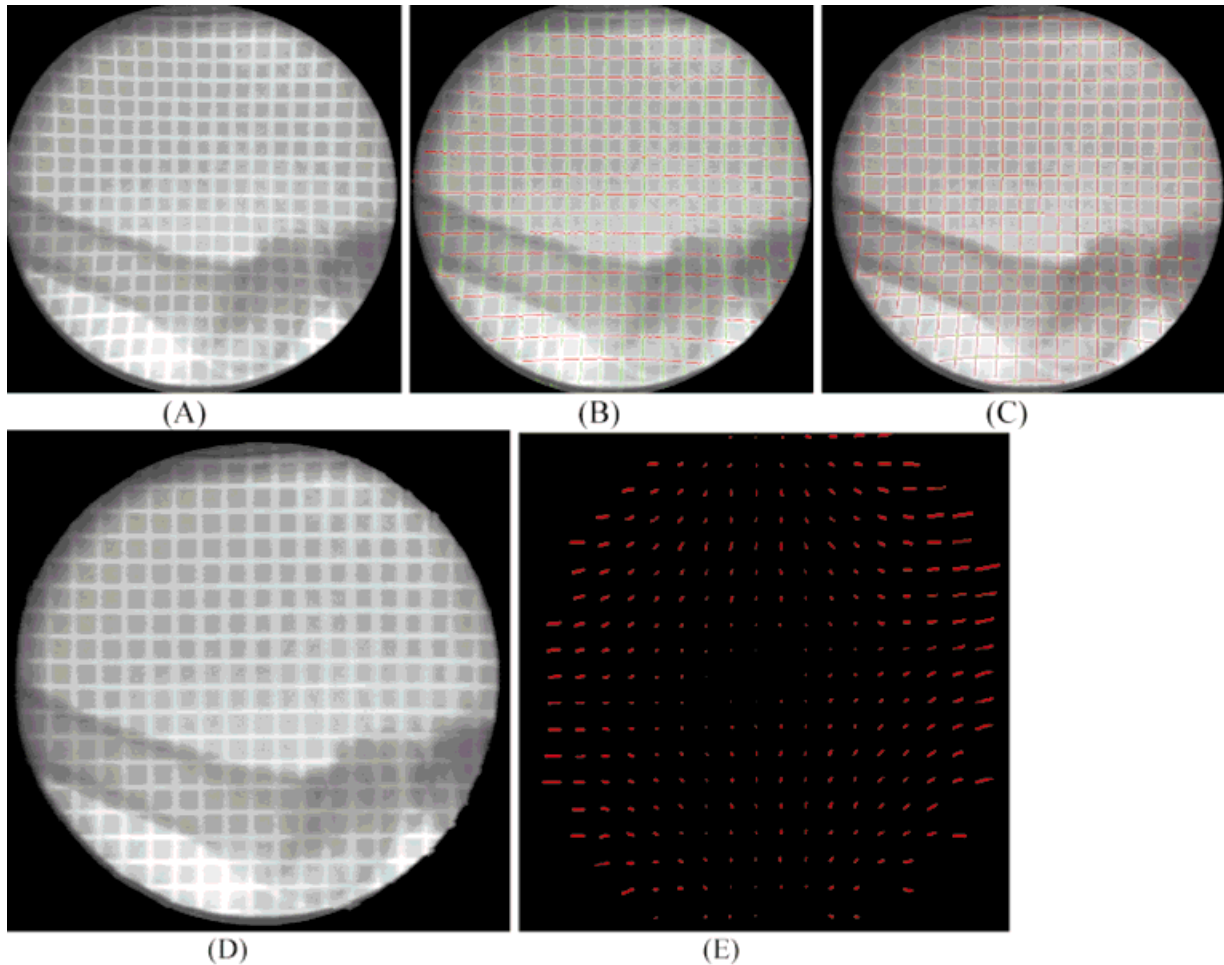


Fig. 4. Image de-warping experiment. (A) Fluoroscopic X-ray image of a smoked ham (the radio density of the ham is similar to that of a human thigh); (B) the groove points are located using coarse-to-fine strategy; (C) the groove points are fitted into a fifth-order Bernstein-based polynomial; (D) de-warped image; (E) the distortion vector graph over the image space.

cylinder shape with steel beads on it, and can be mounted directly on the image intensifier plate. Guezic et al.¹² extended the “NPBS” method to provide a method that combined the fluoroscopic image de-warping and calibration.

An important feature of our current research is that it provides image-based methods for the co-registration of the portable C-arm without an external tracking device. Our strategy relies on identifying features within a single X-ray image of a known 3D arrangement of fiducials and computing the appropriate transformation. We once considered modifying the fixator that holds the femur during PTHR and RTHR to include fiducial lines. One drawback of this approach is that the fixator tends to become more bulky, and would move relative to the femur during the operation. Consequently, we have been considering an alternative

strategy in which a calibration object is held by the robot and placed either inside the femoral cavity or else very close to the bone. Further, since we wish to preserve the ability to use X-rays to monitor progress and update our registration at multiple stages of the cutting procedure, it would be very desirable to integrate the calibration fiducial object directly with the robot or the surgical tools. These considerations have led us to explore a calibration fiducial geometry consisting of a 5/4-turn “corkscrew” spiral and four circular rings surrounding a central shaft, as shown in Figure 5. The initial embodiment was designed to be held in the JHU/IBM LARSTM robot³⁴ or to be mounted on the ROBODOC[®] orthopedic cutter. It is fabricated from autoclavable polyamide with a steel central shaft and copper wire-filled grooves machined into the outside of the polyamide rod. We tested two

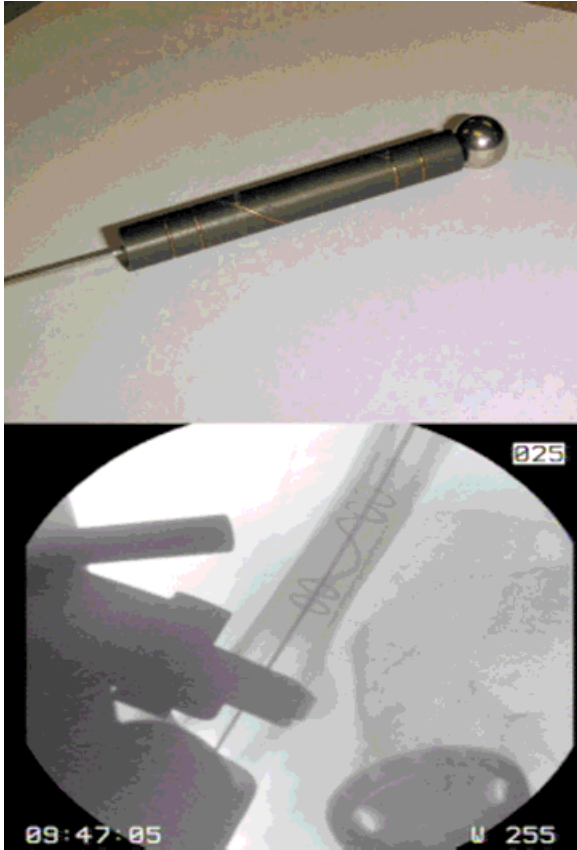


Fig. 5. Corkscrew fiducial object. Top: Corkscrew fiducial object. Bottom: Intra-operative X-ray image of corkscrew object.

methods to attach this corkscrew to the ROBODOC® surgical cutter: one is a holder that positions the corkscrew parallel to the shaft of the cutter, the other is a clamp that holds the corkscrew directly at the end of the cutter. The holders are designed to guarantee that the corkscrew can be replaced at the exact same position relative to the cutter. Both methods provide good results.

The geometry of the corkscrew has the property that its 6D pose [3 translations (X, Y, Z) and 3 rotation angles (α, β, γ)] can be computed from a single 2D perspective projection image. Calculation of the parameters is accomplished by applying image segmentation algorithms and a series of Hough transforms to the subject image, obtaining a subset of the parameters using different parts of the fiducial geometry at each pass. The procedure may be outlined as follows (see Fig. 6):

- The centerline is detected by searching the longest straight line in the image plane using a Hough transform. The centerline of the shaft

provides one rotation and one translation parameter, both in the image plane, restricting the centerline of the fiducial to lie on a plane in 3D space. After the first pass, the searching region is limited to a rectangular area around the line.

- In the limited rectangular searching region, we search for four ellipses along the centerline with the same primary radius and secondary radius by a Hough transform. The distance constraints between rings are also imposed during this search for the ellipses. The ellipses projected by the four rings give the other two translations, as well as a rotation into or out of the plane. The first translation is determined by the position of the pattern of ellipses along the centerline. The distance between the ellipses determines the fiducial's distance from the image plane (the final translation in 3D). The pairs of ellipses allow more robust calculation of these parameters.
- Finally, the phase of the helix can also be detected in the central area between ellipses, again using a Hough transform. The helix provides the final twist rotational component, β . The phase angle of the projection of the helix directly determines this angle. The shape of the projected helix also determines whether the corkscrew rotates into or out of the image plane, i.e., the sign of angle β .

The corkscrew detection algorithm is reasonably robust due to the use of the Hough transforms and the known geometric constraints between different components. Since we can limit our searching region down to a small area after the first pass, the algorithm is very fast and can be finished almost in real time (less than half a second). The corkscrew can be used for pose estimation of C-arm geometry and co-registration between two C-arm poses. By attaching this corkscrew to the robot's end-effector (or surgical tool) and conducting a preoperative corkscrew-robot registration, the registration between the robot and the imager can also be computed.

After finding and computing the geometry parameters of the corkscrew projection on the 2D image, the transformation between the image coordinate system (O) and the corkscrew coordinate system (O') can be constructed (Fig. 6). As in Figure 6, the twist angle α is equal to the phase of the helix. The roll angle β (the angle of the corkscrew rotation into or out of the image plane) can be written as

$$a \sin\left(\frac{\text{primary radius of ellipse}}{\text{secondary radius of ellipse}}\right),$$

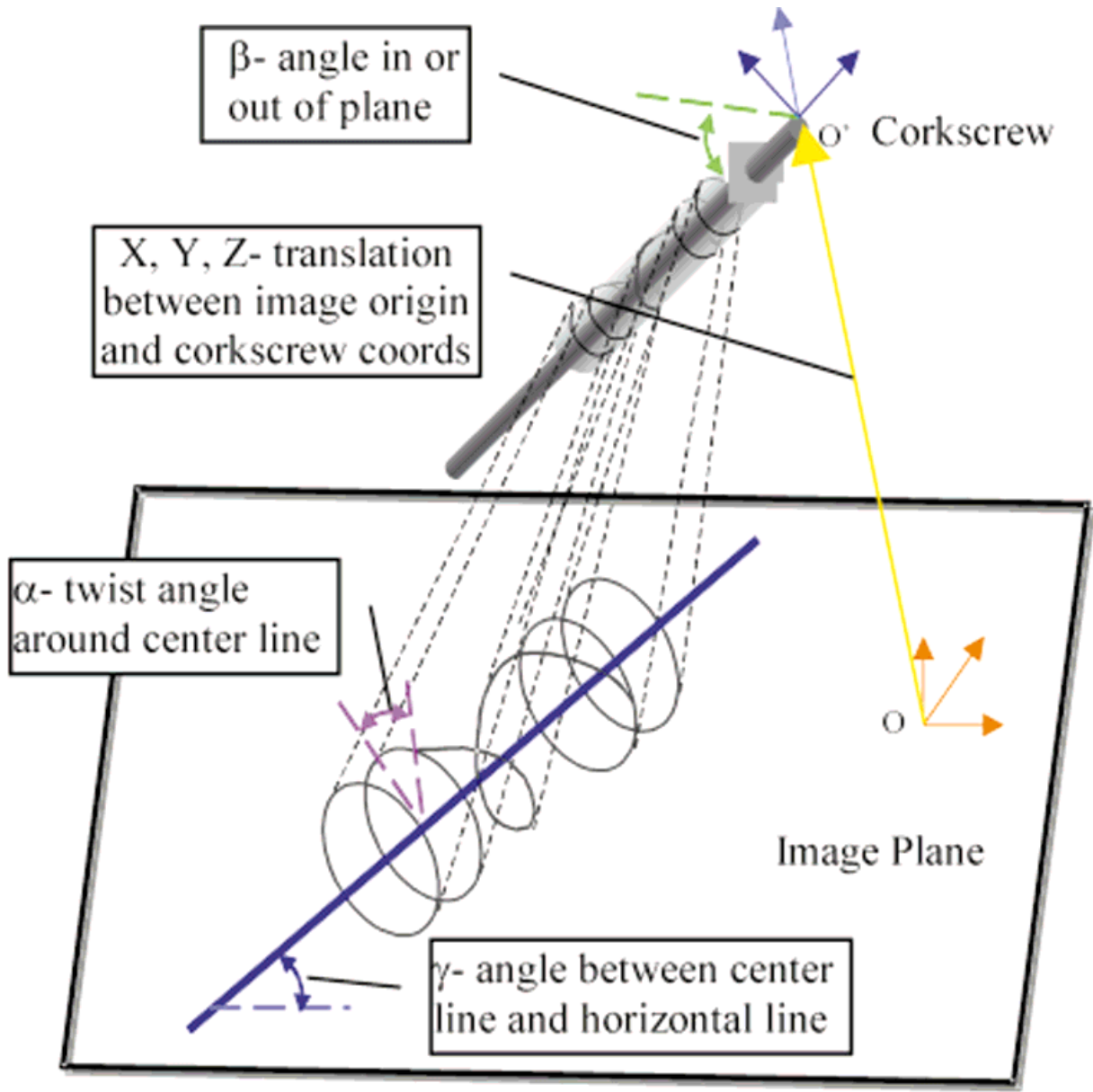


Fig. 6. 2D projection of corkscrew.

and the shape of the helix determines the sign of β . The pitch angle γ is the angle between the corkscrew axis and the horizontal scan line of the

image plane. Thus, the rotation R between these two frames can be constructed using Z-Y-X Euler angles (γ, β, α) as in Equation (6):

$$R = R_Z(\gamma)R_Y(\beta)R_X(\alpha)$$

$$= \begin{bmatrix} \cos \gamma \cos \beta & \cos \gamma \sin \beta \sin \alpha - \sin \gamma \cos \alpha & \cos \gamma \sin \beta \cos \alpha + \sin \gamma \sin \alpha \\ \sin \gamma \cos \beta & \sin \gamma \sin \beta \sin \alpha + \cos \gamma \cos \alpha & \sin \gamma \sin \beta \cos \alpha - \cos \gamma \sin \alpha \\ -\sin \beta & \cos \beta \sin \alpha & \cos \beta \cos \alpha \end{bmatrix} \quad (6)$$

Table 1. Rotation Error Assessment in Corkscrew Pose Estimation Method from a Single Viewpoint

Trial	Robot twist angle	Computed twist angle	Error (°)	Robot roll angle	Computed roll angle	Error (°)	Robot pitch angle	Computed pitch angle	Error (°)	
1	30	30.28	0.28	15	17.26	2.26	15	14.82	0.18	
2	60	59.53	0.47	30	31.76	1.76	30	29.34	0.66	
3	90	88.95	1.05	45	44.17	0.83	45	47.07	2.07	
4	120	120.64	0.64	-15	-12.31	2.69	-15	-13.84	1.16	
5	150	149.74	0.26	-30	-31.82	1.82	-30	-30.28	0.28	
Average error			0.54°				1.87°			
Standard deviation			0.32°				0.69°			

The translation $T (T_x, T_y, T_z)$ between two frames can be computed using Equation (7),

$$\frac{T_x}{T_{x'}} = \frac{l \cos \beta}{l'}, \quad \frac{T_y}{T_{y'}} = \frac{l \cos \beta}{l'}, \quad \frac{f - T_z}{f} = \frac{l \cos \beta}{l'} \quad (7)$$

where f is the focal length, l is the physical length of the corkscrew, l' is the projected length of the corkscrew computed from the image, and $(T_{x'}, T_{y'})$ is the 2D translation of the corkscrew in the image plane.

We conducted the following experiments to assess the accuracy of our corkscrew pose estimation method. The corkscrew was mounted on the LARS™ robot's end-effector such that the axis of the corkscrew coincided with the axis of the robot end-effector. First, one image of the corkscrew was taken. Then, keeping the C-arm pose unaltered, the robot was translated or rotated (only one joint was moved each time to isolate the error) and another image was taken after the movement. The corkscrew movement (i.e., the movement of the robot end-effector) between the two images was computed based on the pose estimation algorithm. Because the LARS™ robot's precision is about 20 μm and 0.01°, the computed movement was compared to the known movement of the robot to assess the accuracy of the corkscrew registration method. Ta-

bles 1 and 2 show the results. The results indicate that the rotation accuracy of the registration method is around 1–2 degrees. The error of the roll angle is large because the secondary radius of the ring cannot be computed accurately, especially when the angle is small. The results also show that the average translation error is under 0.5 mm along the directions parallel to the image plane (axes x and y), and can be larger than 1.0 mm along the focal length direction (axis z). Currently, a constant focal length is assumed for this step. This contributes to the error of the translation along the focal length direction. The accuracy obtained is reasonable for an image-based registration method, but may not be good enough for a surgical system. Although we could improve the extrinsic parameter estimation by changing the corkscrew design (e.g., increasing its diameter or picking a different shape), we have chosen to investigate a progressive strategy using feedback to improve accuracy. The advantage of such an approach is that it is generally applicable in cases where the local precision of image processing and the robot is superior to whatever absolute registration accuracy can be achieved.

Initial Cutting Experiments

We have conducted some cutting experiments using the orthopedic cutter and dental acrylic phantoms. Tests were carried out on phantoms in order

Table 2. Translation Error Assessment in Corkscrew Pose Estimation Method from a Single Viewpoint

Trial	Robot translate X	Computed translate X	Error (mm)	Robot translate Y	Computed translate Y	Error (mm)	Robot translate Z	Computed translate Z	Error (mm)	
1	5	5.04	0.04	5	5.13	0.13	5	5.61	0.61	
2	10	9.73	0.27	10	10.39	0.39	10	11.25	1.25	
3	15	14.2	0.8	15	14.35	0.65	15	13.62	1.38	
4	-5	-5.13	0.13	-5	-5.18	0.18	-5	-5.42	0.42	
5	-10	-9.93	0.07	-10	-9.76	0.24	-10	-10.96	0.96	
Average error			0.26				0.32			
Deviation			0.31				0.21			

to verify basic system accuracy and to gain confidence in overall system behavior. The following is a general procedure for a cutting experiment.

Step 1: The corkscrew is attached to the cutter mounted on the robot end-effector. A separate procedure is performed to calibrate the robot and the corkscrew, i.e., to compute $F_{robot-corkscrew}$.

Step 2: Several images (typically two images) of the corkscrew and the femur (phantom) are taken. Then the registration, $F_{corkscrew-imager}$, between the corkscrew and the imager is computed using the corkscrew pose estimation algorithm described in the section entitled *C-arm pose estimation and extrinsic calibration*. The registration $F_{femur-imager}$ between the femur and the imager is obtained using the femur anatomy or fiducial beads (at present fiducial beads are used). Finally the registration between femur and robot is written as

$$F_{robot-femur} = F_{robot-corkscrew} \cdot F_{corkscrew-imager} \cdot F_{imager-femur}$$

Step 3: The cutter is moved to the starting position, and a predefined shape is cut. At present, a constant-orientation cutting strategy is employed and a cubic staircase pocket is machined at the center of the phantom along the long axis of the phantom.

The cavity position error was determined by measuring wall thickness using calipers. With an angular separation of about 50 degrees between two C-arm views, we observed a cavity placement error of around 0.5 mm to 1.5 mm. A number of factors may account for the errors in this initial registration. To begin with, the elderly Polarix 2 fluoroscope being used in these experiments provides relatively poor resolution, resulting in small errors in location of the fiducial patterns (both corkscrew and beads). In addition, the robot configuration being used for these experiments provides only translational degrees of freedom. Therefore, the assumption is made that the axis of the cutter, the x-axis of the robot, the central axis of the coil, and the axis of the phantom are all exactly collinear. Since no control is available to correct for misalignments between these axes, small deviations from this assumption can result in significant positioning error. In any case, these results led us to explore a progressive cutting strategy described in the next two sections.

Cavity Location Algorithm

We are investigating a progressive cut refinement strategy to improve the cavity placement accuracy.

First a small cavity is cut, then a cavity location algorithm is applied to compute the discrepancy between the real cut pocket and the cut model, and the registration between the robot and femur anatomy is adjusted accordingly. During the next cut, a larger pocket is milled and the process is repeated until the final desired shape has been cut. The progressive cut refinement strategy is practical, because in present ROBODOC® PTHR surgery, the cavity is already milled in similar stages.

The idea of progressive cutting is straightforward. The problem is how to measure the error after each cut using the fluoroscopic C-arm. We developed the following cavity location algorithm to solve this problem. The 3D surface model of the cut cavity (a list of triangular facets) and its transformation relative to the femur is planned in the preoperative stage. After one progressive cut, several images of the cut cavity and corkscrew are taken from different view angles. The C-arm geometry of each image is constructed using the corkscrew pose estimation algorithm. At each pose, an image subtraction technique is employed to generate the 2D contour of the cut cavity, denoted as C_c . The projective apparent contour C_m of the surface model of the cut cavity is then built. A 2D contour registration algorithm is applied to get the 2D transformation between C_c and C_m , then the transformation between the real cut cavity and the cut model is updated according to the 2D transformation obtained. The above procedure is iterated at each C-arm pose to compute the estimated transformation between the real cut cavity and the cut model. Finally, this transformation is used to update the registration between the robot and the femur.

Projective Apparent Contour of 3D Surface Model

An algorithm for generating the 2D projective apparent contour of a 3D surface model under known view geometry was developed. The 3D surface model is a list of 3D triangular facets. Given the view geometry (center of perspective and viewing direction), each facet on the surface is evaluated. If its normal makes an obtuse angle with the viewing direction, then the facet is said to be visible; otherwise, it is invisible. The projective apparent contour is then the projection of the set of edges on the surface, such that the facet on one side of the edge is visible while the facet on the other side of the edge is invisible. To efficiently compute the projective apparent contour, the 3D surface model is stored in a winged edge data structure.

Figure 7 shows some results of our algorithm.



Fig. 7. Projective contour of 3D model.

The left side image is a 3D model of an implant. The right side image is its 2D projective contour.

2D Contour Registration Algorithm

The method used in the contour registration is derived from the Principal Component Analysis method.³⁵ There are two stages in the computation of the 2D transformation between two 2D projective contours. During the first stage, the initial 2D transformation between the contours is computed using first and second order moments. The following are some formulas defining the 2D moments:

First Order Moment:

$$Mean = (\bar{x}, \bar{y}) = \frac{1}{n} \sum_{i=1}^n (x_i, y_i),$$

where (x_i, y_i) is i th point on the contour

Second Order Moment:

Inertia Matrix

$$= \begin{pmatrix} \sum_{i=1}^n (x_i - \bar{x})^2 & \sum_{i=1}^n (x_i - \bar{x})(y_i - \bar{y}) \\ \sum_{i=1}^n (x_i - \bar{x})(y_i - \bar{y}) & \sum_{i=1}^n (y_i - \bar{y})^2 \end{pmatrix}$$

The initial translation is then $Mean_1 - Mean_2$. The eigenvectors of the inertia matrix are very meaningful (see Fig. 8), so the angle between the corresponding eigenvectors can be regarded as the initial rotation angle between the two contours.

The second stage is an ICP (Iterative Closet Point) algorithm. It involves using the Least-Square-Error method to recursively update the transformation. Basically, for each point p_i on contour 1, the closest point q_i on contour 2 is found, and by minimizing the distance

$$\min_{R,t} \sum_{i=1}^n d_i^2 = \min_{R,t} \sum_{i=1}^n \|Rp_i + t - q_i\|^2,$$

R and t can be solved. Since the complete contour is used, the initial transformation obtained in the first stage can bring the two contours very close. It usually takes two or three iterations to converge in the ICP stage.

Digital Subtraction

On the image of the cut cavity, the edge of the cavity is often blurred. It is impractical and inaccurate to rely on an edge detector or image gradient method to detect the contour of the cavity. We instead turned to a digital subtraction technique for the solution.³⁶

The procedure for utilizing digital subtraction is as follows:

1. A set of images are acquired before cutting begins. The pose of the C-arm corresponding to each image is noted. Currently, this is done by simply marking the positions of each C-arm joint with a pencil.
2. After cutting, the C-arm is returned as closely as possible to each previous pose and a second set of images is acquired. In our experience, it is easy to ensure that the difference between the first and second poses is in the order of 4 cm and 5°.
3. The corkscrew fiducial and the outer contour of the phantom are used to obtain the difference between the C-arm poses of the two sets of images (Figs. 9 and 10).
4. The images from before the cut are then aligned with the images from after the cut (Fig. 9). The alignment is a 2D transformation including translation, rotation and scaling.

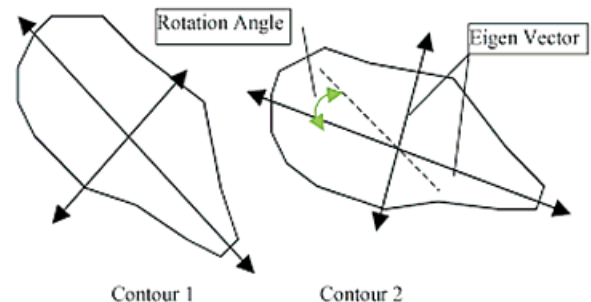


Fig. 8. Second-order moments of contours.

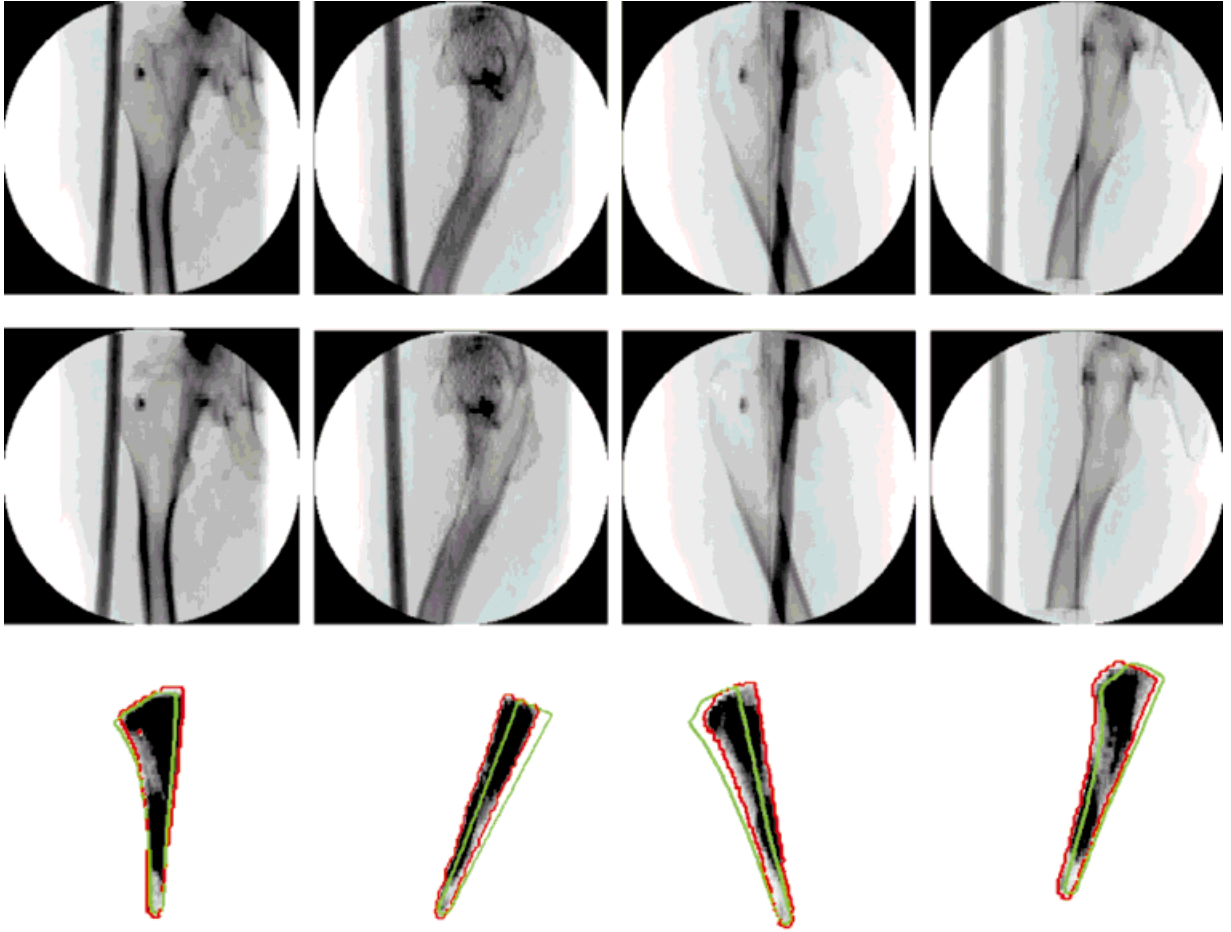


Fig. 9. Images used on Cavity Location Algorithm. Row 1 are images-before-cut; row 2 are images-after-cut; and row 3 are their subtractions after removing the noises and enhancing the contrast, superimposed with the contours of the real cavity (red lines) and projective model contours (green line).

5. The second set of images are subtracted from the initial images. The 2D contour of the cavity on the subtraction image can be generated using a Snake algorithm³⁷ or a marching square algorithm.³⁸

The digital subtraction of these two images can provide meaningful information. Using our image alignment method, we can eliminate most of the structure noises in image subtraction caused by the slightly different C-arm poses before and after cutting.

Computational Analysis

The objective of the cavity location algorithm is to compute ΔF , i.e., to compute the transformation between the cut cavity and the planned cavity model.

The transformation between the planned cavity model and the C-arm coordinate system can be written as $F_{v-m} = F_v^{-1}F_m$, where F_v is the C-arm coordinate frame, and F_m is the planned cavity model coordinate frame. Based on F_{v-m} , the projective contour C_m of the model is generated, then the 2D contour transformation algorithm is employed to get the 2D translation $(\Delta x, \Delta y)$, 2D rotation angle $\Delta\theta$, and the rotation center (x_0, y_0) .

Distance from the cavity model to the C-arm source along the focal length direction can be written as $d = (F_m.P - F_v.P) \circ F_v.R.Rz$, where $F_v.R.Rz$ is the viewing direction, and \circ is the dot product between two vectors.

The 3D transformation between the cut cavity and the planned cavity model $\Delta F_c = T_2^{-1}R_1T_2T_1$, where

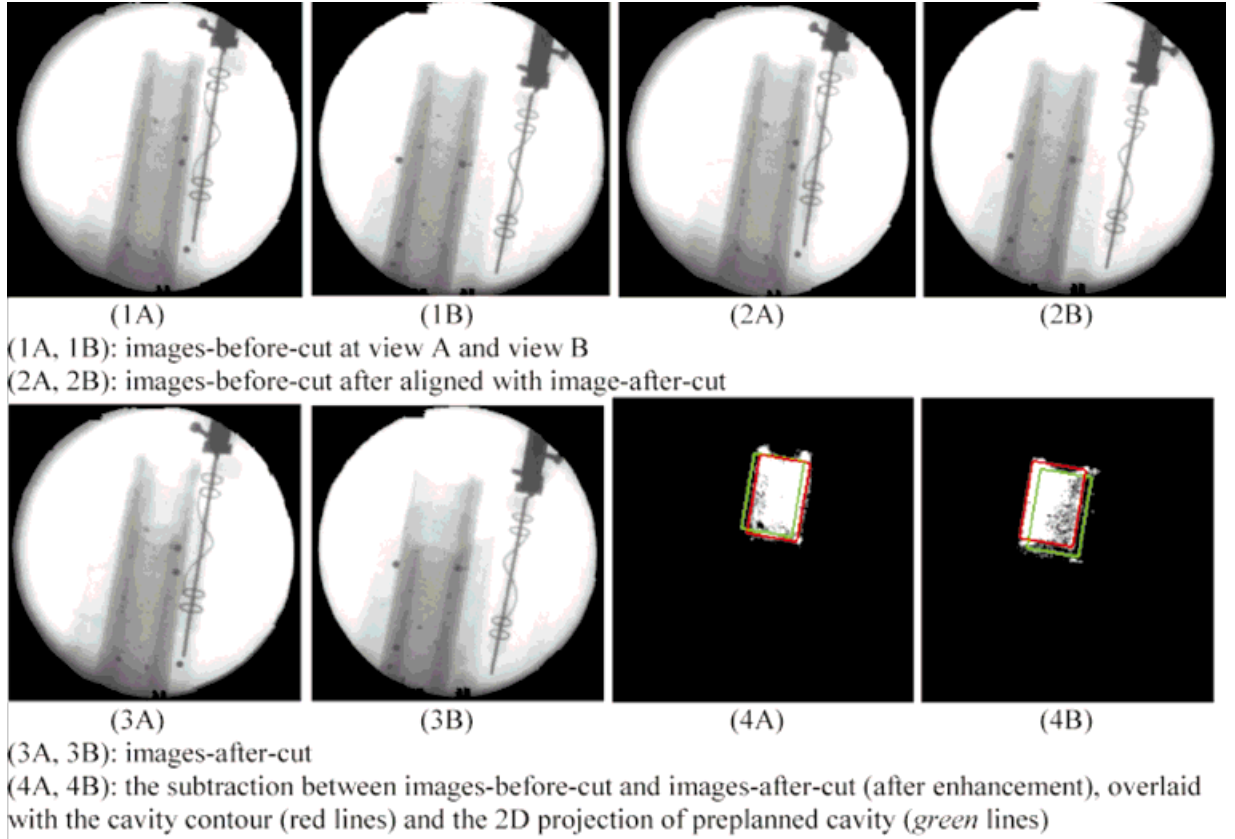


Fig. 10. Image subtraction results.

$$T_1 = \text{Translate} (\Delta x \cdot s_x \cdot d/f, \Delta y \cdot s_y \cdot d/f, 0)$$

$$R_1 = \text{Rotation} (\Delta\theta, Z\text{-axis})$$

$$T_2 = \text{Translate} (x_0 \cdot s_x \cdot d/f, y_0 \cdot s_y \cdot d/f, 0)$$

Here, f is the focal length of the C-arm and (s_x, s_y) is the pixel size of the 2D image. So the cumulative transformation ΔF_w can be denoted as

$$\Delta F_w.P = F_v.R \cdot \Delta F_c.P \text{ and}$$

$$\Delta F_w.R = F_v.R \cdot \Delta F_c.R$$

Then the Cavity Model frame and the cumulative transformation can be updated by:

$$F_m = \Delta F_w \cdot F_m \text{ and } \Delta F = \Delta F_w \cdot \Delta F.$$

The above computing procedure is iterated on all images. Finally, the transformation between the cut cavity and the planned cavity model is obtained. In our algorithm, quaternions are used to represent the rotations.

Progressive Cutting Experiments

We have tested our progressive cutting strategy on simulated images and on dental acrylic phantoms in cutting experiments.

Simulation Experiments

We have implemented software to generate a simulated fluoroscopic image from a CT data volume based on standard attenuation rules. The method used is a simplified ray-tracing algorithm, i.e., for every pixel on the image plane, a ray is shot from the source to the pixel and the attenuation along that ray is computed and used as the gray level of that pixel. The simulated image is very realistic, except that there is no spatial distortion (this is reasonable, because the distortion needs to be corrected anyway). Subtracting the cavity volume from the CT volume can also simulate the process of cutting a predefined cavity from the CT volume. Figure 9 is a set of simulation images generated from a CT set of a patient femur.

Table 3 provides some numerical assessment of our cavity location method. During this experi-

Table 3. Results of Cavity Location Algorithm

Trial	Expected transformation (mm)						Computed transformation (°)						Translation error (mm)	Rotation error (°)
	X	Y	Z	Roll	Pitch	Yaw	X	Y	Z	Roll	Pitch	Yaw		
1	2.00	1.00	0.00	0.00	0.00	0.00	1.93	1.05	0.01	0.00	0.00	0.00	0.09	0.00
2	-2.00	1.50	1.00	0.00	0.00	0.00	-2.09	1.42	0.94	0.03	0.00	-0.01	0.13	0.03
3	0.00	0.00	0.00	2.00	4.00	-2.00	0.06	0.03	-0.02	2.30	3.54	-0.57	0.07	1.53
4	0.00	0.00	0.00	-3.00	3.00	3.00	0.11	-0.05	0.07	-2.18	3.49	1.67	0.14	1.64
5	1.00	-2.00	-3.00	3.00	2.00	2.00	0.56	-2.21	-3.30	2.47	2.37	0.43	0.57	1.70
												Average	0.20	0.98
												Std Dev	0.21	0.88

ment, a cut cavity (in the shape of an implant) is first preplanned relative to the femur. A perturbation transformation is applied to the pose of the preplanned cut cavity to simulate the registration error between the preplanned shape and the cutting device, and a simulated cutting of the perturbed cavity is executed on the femur. Furthermore, the images-before-cut and the images-after-cut are computed from slightly different C-arm geometries to simulate the structural noises caused by non-identical C-arm poses before and after the cut. The structural noise in the image subtraction (see *Digital Subtraction* section above) is eliminated by the 2D alignment using the outer contour of the femur. The Cavity Location algorithm is then employed to recover the perturbation transformation. Figure 9 illustrates the images simulated in trial 5 of Table 3. From Table 3, we find that the perturbation transformation can be mostly restored.

Phantom Experiments

Several phantom cutting experiments have been done to verify our registration technique and progressive cutting strategy. The experiments are outlined as following:

0. Perform the initial registration using the technique described in the *C-arm Calibration and Pose Estimation* section.
1. Take two images-before-cut at two different predetermined C-arm poses.
2. Cut a preplanned shape.
3. Move the C-arm back through the predetermined poses, taking an image-after-cut at each pose.
4. Align each image-before-cut with the corresponding image-after-cut with the aid of the corkscrew and the outer contour of the phantom, since they aren't taken at exactly the same C-arm pose.
5. Subtract each image-after-cut from the corresponding images-before-cut. (Note: each

of these images was aligned in the previous step.)

6. From the subtraction images, detect the contour of the cut cavity and compute the 2D transformation between the contour of the cut cavity and the 2D projection of the preplanned cavity.
7. Back-project the 2D transformations into 3D space and obtain the 3D transformation between the cut cavity and the preplanned cavity.
8. Revise the robot-phantom registration and the preplanned shape according to the 3D transformation computed in step 7, and re-iterate from step 1 to step 7.

Figure 10 shows the intermediate results of the phantom cutting experiment. The results presented in Table 4 shows the offsets between the cut cavity and preplanned cavity. In this experiment, we planned the cut cavity as a cubicle cavity in the center of the phantom. After each cut, we measured the thickness of the wall using calipers to compute the offset between the cut cavity and the planned cavity. We conducted three trials. In the first two trials we tried two iterations, and we ran three iterations in the third trial. In Table 4, we show the cavity size and the offsets along the x and y axes of the phantom. From the results, we find that the progressive cutting strategy can reduce the offsets (registration error) down to around 0.5 mm after two iterations.

DISCUSSION AND FUTURE PLANS

The system and method described in this paper demonstrate the feasibility of cutting a precise pocket using C-arm fluoroscopy. We have been able to demonstrate an order of magnitude improvement in precision by the progressive refinement strategy, as compared to image-based methods without progressive refinement, in RTHR surgery. Based on the preliminary results, our re-

Table 4. Offsets between Cut Cavity and Preplanned Cavity at Each Iteration (in mm)

Trial	First cut			Second cut			Third cut		
	Cavity size	Offset (X, Y)		Cavity size	Offset (X, Y)		Cavity size	Offset (X, Y)	
1	18*18*40	-2	-0.25	23*23*40	-0.64	-0.2	N/A	N/A	N/A
2	18*18*40	-1.604	0.295	23*23*40	-0.13	-0.255	N/A	N/A	N/A
3	15*15*40	2.1	1.3	20*20*40	0.95	0.515	22*22*40	0.35	0.025

search shows that a fluoroscopy-based registration method and progressive cutting strategy is a promising alternative for RTHR, as well as other orthopedic surgery procedures.

In fact, these methods have been shown to work surprisingly well considering the very old imaging equipment that we used for the investigations reported here. We chose this equipment because it was readily available for extended periods, thus facilitating ongoing experiments. Clearly, one future step will be to evaluate these and similar techniques on more modern equipment. This will be a natural consequence of the steps taken toward eventual clinical use, as well as of future investigations of these basic ideas in a variety of other applications at Johns Hopkins University and elsewhere.

A number of areas must be further investigated, including the anatomy-based registration methods. We plan to further assess the accuracy of the corkscrew pose estimation algorithm under different circumstances. We also plan to integrate an independent validation system using the Optotrak® system to assess the accuracy of our system, to conduct further studies on dry bones and cadavers, and—eventually—to integrate our system into the OR for patient trials.

ACKNOWLEDGMENT

This work was partially funded by NIST Advanced Technology Program Cooperative Agreement No. 94-01-0228, in cooperation with Integrated Surgical Systems (ISS) and IBM. It also benefited from NSF equipment grants CDA-9529509 and EIA9703080, and from an equipment grant from Intel. We thank our colleagues from IBM and ISS for their collaboration in all phases of this research. Leo Joskowicz, Alan Kalvin, Bill Williamson, and Brent Mittelstadt perhaps deserve special thanks, as does Rod Turner, M.D., from New England Baptist Hospital.

Two of the authors (Van Vorhis and Kazanzides) are employees of Integrated Surgical Systems. Another author (Taylor) is a member of the Scientific Advisory Board of ISS and consequently has a small financial interest in ISS.

REFERENCES

1. Taylor RH, Joskowicz L, Williamson B, Guezic A, Kalvin A, Kazanzides P, Van Vorhis R, Yao J, Kumar R, Bzostek A, Sahay A, Börner M, Lahmer A. Computer-integrated revision total hip replacement surgery: concept and preliminary results. *Med Image Anal* 1999;3:301–319.
2. Skibbe H, Börner M, Wiesel U, Lahmer A. Revision THR using the ROBODOC system. In: CAOS/USA '99. Third Annual North American Program on Computer Assisted Orthopaedic Surgery, Pittsburgh, Pennsylvania, June 17–19, 1999. p 110–111.
3. Bauer A. Primary THR using the ROBODOC system. In: CAOS/USA '99. Third Annual North American Program on Computer Assisted Orthopaedic Surgery, Pittsburgh, Pennsylvania, June 17–19, 1999. p 107–108.
4. Petermann J, Kober R, Heinze P, Heeckt PF, Gotzen L. Implementation of CASPAR system in the reconstruction of the ACL. In: CAOS/USA '99. Third Annual North American Program on Computer Assisted Orthopaedic Surgery, Pittsburgh, Pennsylvania, June 17–19, 1999. p 86–87.
5. Joskowicz L et al. Computer integrated revision total hip replacement surgery: preliminary report. In: Proceedings of the Second Annual International Symposium on Medical Robotics and Computer Assisted Surgery (MRCAS '95), Baltimore, Maryland, 1995. New York: Wiley, 1995. p 193–202.
6. Taylor RH et al. An image-directed robotic system for precise orthopaedic surgery. *IEEE Transact Robot Automat* 1994;10:261–275.
7. Wiesel U, Lahmer A, Börner M, Skibbe H. ROBODOC at Berufsgenossenschaftliche Unfallklinik Frankfurt—Experiences with the Pinless System. In: CAOS/USA '99. Third Annual North American Program on Computer Assisted Orthopaedic Surgery, Pittsburgh, Pennsylvania, June 17–19, 1999. p 113–117.
8. Lavallée S, Szeliski R, Brunie L. Anatomy-based registration of three-dimensional medical images, range images, X-ray projections, and three-dimensional models using octree-splines. In: Taylor RH, Lavallée S, Burdea GC, Mösges R, editors: *Computer-Integrated Surgery: Technology and Clinical Applications*. Cambridge MA: MIT Press, 1995. p 115–144.
9. Hamadeh A, et al. Towards automatic registration between CT and X-ray images: cooperation between

- 3D/2D registration and 2D edge detection. In: Proceedings of the Second Annual International Symposium on Medical Robotics and Computer Assisted Surgery (MRCAS '95), Baltimore, Maryland, 1995. New York: Wiley, 1995. p 39–46.
10. Gueziec A, Kazanzides P, Williamson B, Taylor RH. Anatomy based registration of CT-scan and intra-operative X-ray images for guiding a surgical robot. *IEEE Transact Med Imaging* 1998;17:715–728.
 11. Gueziec A, Kazanzides P, Williamson B, Taylor RH, Lord D. Anatomy based registration of CT-scan and X-ray fluoroscopy data for intra-operative guidance of a surgical robot. In: Hanson KM, editor: *Medical Imaging 1998: Image Processing*. SPIE Proceedings Vol. 3338, 1998. p 81–94.
 12. Gueziec AP, et al. Registration of computed tomography data to a surgical robot using fluoroscopy: a feasibility study. 1996.
 13. Hamadeh A, Lavallée S, Szeliski R, Cinquin P, Peria O. Anatomy-based registration for computer-integrated surgery. In: Ayache N, editor: *Computer Vision, Virtual Reality, and Robotics in Medicine*. Lecture Notes in Computer Science Vol. 905. Berlin: Springer, 1995. p 212–218.
 14. Liu A, Bullitt E, Pizer SM. 3D/2D registration via skeletal near projective invariance in tubular objects. In: Wells WM, Colchester A, Delp S, editors: *Proceedings of First International Conference on Medical Image Computing and Computer-Assisted Intervention (MICCAI '98)*, Cambridge, MA, October 1998. Berlin: Springer, 1998. p 952–963.
 15. Weese J, Buzug TM, Lorenz C, Fassnacht C. An approach to 2D/3D registration of a vertebra in 2D X-ray fluoroscopies with 3D CT images. In: Troccaz J, Grimson E, Mösges R, editors: *Proceedings of First Joint Conference on Computer Vision, Virtual Reality and Robotics in Medicine and Medical Robotics and Computer Assisted Surgery (CVRMed-MRCAS '97)*, Grenoble, France, March 1997. Berlin: Springer, 1997. p 119–128.
 16. Wells WM, Viola P, Kikinis R. Multi-model volume registration by maximization of mutual information. In: *Second Annual International Symposium on Medical Robotics and Computer Assisted Surgery (MRCAS '95)*, Baltimore, Maryland, 1995. New York: Wiley; 1995. p 39–46.
 17. Gueziec AP, Funda J. Evaluating the registration of 3D points to 3D lines with application to the pose estimation in a projective image. 1996.
 18. Gueziec A. Assessing the registration of CT-scan data to intra-operative X-rays by fusing X-rays and preoperative information. *Proc SPIE Med Imaging* 1999. p 3661–3688.
 19. Champléoux G et al. Accurate calibration of cameras and range imaging sensors, the NPBS method. *Proceedings of the IEEE International Conference on Robotics and Automation*, 1992. p 1552–1557.
 20. Bookstein FL. *Morphometric Tools for Landmark Data, Geometry and Biology*. Cambridge University Press, 1991.
 21. IS Systems. *ORTHODOC User Guide*. 1997.
 22. Nolte LP et al. Use of C-arm for surgical navigation in the spine. In: *CAOS/USA '98*. Second Annual North American Program on Computer Assisted Orthopaedic Surgery, Pittsburgh, Pennsylvania, 1998.
 23. Phillips R et al. Image guided orthopaedic surgery—design and analysis. *IEEE Transact Robot Control*, March 1996.
 24. Hofstetter R, Slomczykowski M, Sati M, Nolte L-P. Principles of precise fluoroscopy based surgical navigation (abstract). In: *4th International Symposium on Computer Assisted Orthopaedic Surgery*, Davos, Switzerland, March 1999. p 28.
 25. Hofstetter R, Slomczykowski M, Bourquin I, Nolte L-P. Fluoroscopy based surgical navigation—concept and clinical applications. In: Lemke HU, Vannier MW, Inamura K, editors: *Computer Assisted Radiology and Surgery*. Proceedings of the 11th International Symposium and Exhibition (CAR '97), Berlin, Germany, June 1997. Amsterdam: Elsevier, 1997. p 956–960.
 26. Brack C, Burgkart R, Czopf A, Götte H, Roth M, Radig B, Schweikard A. Accurate X-ray-based navigation in computer-assisted orthopedic surgery. In: Lemke HU, Vannier MW, Inamura K, Farman AG, editors: *Computer Assisted Radiology and Surgery*. Proceedings of the 12th International Symposium and Exhibition (CAR '98), Tokyo, Japan, June 1998. Amsterdam: Elsevier, 1998. p 716–722.
 27. Tsai RY. A versatile camera calibration technique for high-accuracy 3D machine vision metrology using off-the-shelf TV cameras and lenses. *IEEE J Robot Automat* 1987;RA-3(4):323-358.
 28. Schreiner S, Anderson JH, Taylor RH, Funda J, Bzostek A, Barnes AC. A system for percutaneous delivery of treatment with a fluoroscopically-guided robot. In: Troccaz J, Grimson E, Mösges R, editors: *Proceedings of First Joint Conference on Computer Vision, Virtual Reality and Robotics in Medicine and Medical Robotics and Computer Assisted Surgery (CVRMed-MRCAS '97)*, Grenoble, France, March 1997. Berlin: Springer, 1997. p 747–756.
 29. Fahrig R, Moreau M, Holdsworth D. Three-dimensional computed tomographic reconstruction using a C-arm mounted XRII: correction of image intensifier distortion. *Med Phys* 1997;24:1097–1106.
 30. Boone JM, Seibert JA, Barrett WA, Blood EA. Analysis and correction of imperfections in the image intensifier-TV-digitizer imaging chain. *Med Phys* 1991;18:236–242.
 31. Yaniv Z, Joskowicz L, Simkin A, Garza-Jinich M, Milgrom C. Fluoroscopic image processing for computer-aided orthopaedic surgery. In: Wells WM, Colchester A, Delp S, editors: *Proceedings of First International Conference on Medical Image Computing and Computer-Assisted Intervention (MICCAI*

- '98), Cambridge, MA, October 1998. Berlin: Springer, 1998. p 325–334.
32. Wolberg G. Digital Image Warping. IEEE Comput Soc Press Monogr, 1990.
 33. Joskowicz L, Milgrom C, Simkin A, Tockus L, Yaniv Z. FRACAS: A system for computer-aided image-guided long bone fracture surgery. *Comp Aid Surg* 1998;3:271-288.
 34. Taylor RH, Funda J, Eldridge B, Larose D, Gomory S, Gruben K, Talamini M, Kavoussi L, Anderson J. A telerobotic assistant for laparoscopic surgery. In: Taylor RH, Lavallée S, Burdea GC, Mösges R, editors: *Computer-Integrated Surgery: Technology and Clinical Applications*. Cambridge MA: MIT Press, 1995. p 581–592.
 35. Jolliffe IT. *Principal Component Analysis*. Berlin: Springer Verlag, 1986.
 36. Levy G. Robotic control for digital subtraction radiography. In: *Electrical Engineering*. New Brunswick, NJ: Rutgers, the State University of New York, 1994. p 145.
 37. Kass M, Witkin A, Terzopoulos D. Snakes: Active contour models. *Int J Comput Vision* 1987;1:321–331.
 38. Schroeder W, Martin K, Lorensen B. *The Visualization Toolkit*. Englewood Cliffs, NJ: Prentice Hall, 1998.